Signatures of quantum criticality in pure Cr at high pressure

R. Jaramillo[a], Yejun Feng[b,c], J. Wang[c], and T. F. Rosenbaum[c,1]

[a]School of Engineering and Applied Sciences, Harvard University, Cambridge, MA 02138; [b]The Advanced Photon Source, Argonne National Laboratory, Argonne, IL 60439; and [c]The James Franck Institute and Department of Physics, University of Chicago, Chicago, IL 60637

Edited by Laura H. Greene, University of Illinois at Urbana–Champaign, Urbana, IL, and approved June 28, 2010 (received for review April 13, 2010)

The elemental antiferromagnet Cr at high pressure presents a new type of naked quantum critical point that is free of disorder and symmetry-breaking fields. Here we measure magnetotransport in fine detail around the critical pressure, $P_c \sim 10$ GPa, in a diamond anvil cell and reveal the role of quantum critical fluctuations at the phase transition. As the magnetism disappears and $T \to 0$, the magntotransport scaling converges to a non-mean-field form that illustrates the reconstruction of the magnetic Fermi surface, and is distinct from the critical scaling measured in chemically disordered Cr:V under pressure. The breakdown of itinerant antiferromagnetism only comes clearly into view in the clean limit, establishing disorder as a relevant variable at a quantum phase transition.

antiferromagnetism | spin density waves | electric transport

Competition between magnetic and nonmagnetic states of matter in the zero-temperature limit underlies the emergence of exotic ground states such as non-Fermi liquid metals and unconventional superconductors (1). This observation has motivated several decades of work to understand the physics of magnetic quantum phase transitions (QPT) (2–7). A substantial part of the effort has been directed at the materials science challenges that are inherent to realizing nearly-magnetic states of matter and to the fine tuning of materials so that the phase transitions can be probed systematically. The fundamental limitations that remain are uncertainty over the role of disorder (2, 4, 8), as well as a predilection for first-order transitions that shroud the quantum critical behavior (3, 5). Recent X-ray measurements identified a continuous disappearance of magnetic order in the elemental antiferromagnet Cr near the critical pressure $P_c \sim$ 10 GPa, and concurrent measurements of the crystal lattice across the transition failed to detect any discontinuous change in symmetry or volume (9). These results identify Cr as a stoichiometric itinerant magnet with a continuous QPT—where the effects of the critical point should be manifest—and present a rare opportunity to study quantum criticality in a theoretically tractable system that is free from the effects of disorder. Moreover, the use of hydrostatic pressure as a tuning parameter avoids the introduction of any confounding symmetry-breaking fields.

For the experimentalist, studying elemental Cr shifts the significant technical difficulties from solid state chemistry to high pressure experimentation. Here we report on high-resolution measurements of the electrical resistivity and Hall coefficient of Cr as the system is tuned with pressure in a diamond anvil cell across P_c. Magnetotransport is a sensitive probe of quantum criticality and is widely used to identify and characterize quantum matter (4, 5, 8, 10). At ambient pressure Cr orders antiferromagnetically at the Néel temperature, $T_N(P=0) = 311$ K. Below T_N, electrons and holes form magnetic pairs and condense into a spin density wave (SDW), in a process with strong analogies to the Bardeen-Cooper-Schrieffer (BCS) formulation of electron pairing in superconductors (11). The quantum critical point where $T_N \to 0$ can be reached either through applied pressure or chemical doping. Previous transport measurements of $Cr_{1-x}V_x$, $x = 3.2\%$, under pressure revealed a wide regime of quantum critical scaling in this substitutionally disordered system (8). Doping with electron-poor V to near-critical levels lowered the critical pressure, making P_c accessible with a conventional clamp cell. Accessing the QPT in the pure system, on the other hand, requires high sensitivity measurements on submillimeter single crystals in a diamond anvil cell at low temperature (12, 13).

Results

We present here the results from experimental runs with seven different samples, including two that were studied in fine detail in the critical regime. An overview of the resistivity for $0 < P <$ 10 GPa is shown in Fig. 1*A*. The Néel transition is marked by a sharp upturn in the resistivity, $\rho(T)$, as the reduction in metallic carrier density closely tracks the growth of the energy gap, $g(T)$, just below T_N. This data is analyzed by first subtracting the paramagnetic background resistivity $\rho_{PM}(T)$, yielding the normalized magnetic excess resistivity $\Delta\rho/\rho = (\rho - \rho_{PM})/\rho$. This quantity is then fit to a model function which accounts for the formation of a BCS-like energy gap below T_N and the resulting freezing-out of carriers. This model function was successfully applied in an important early study of Cr under pressure by McWhan and Rice (13). By analyzing $\Delta\rho/\rho$ (see *Methods*) we obtain the phase diagram of Fig. 1*B*. $T_N(P)$ evolves exponentially with pressure for $P < 7$ GPa with the form $T_N(P) = T_{N,0}\exp(-cP)$, $T_{N,0} = 310.9 \pm 0.9$ K, $c = -0.163 \pm 0.001$ GPa^{-1}. Above 7 GPa this BCS-like exponential ground state breaks down as the system approaches the QPT.

The data analysis in the immediate vicinity of the QPT is presented in logical progression in Fig. 2. We plot in Fig. 2*A* the electrical resistivity measured in fine detail in the quantum critical regime. For $T < 50$ K the paramagnetic resistivity displays a dominant T^3 dependence. This is demonstrated in Fig. 2*B* where we plot $\rho(T^3)$, and for each pressure we limit the temperature range to $T > T_N$ in order to emphasize $\rho_{PM}(T)$. The T^3 coefficient b varies by less than 6% between samples and is well described by metallic transport due to phonon scattering in the presence of a weakly inelastic nonphonon scattering channel (14). Theory gives $b/d = (4.8/\Theta^2) = 1.74 \times 10^{-5}$ K^{-2}, where Θ is the Debye temperature ($\Theta = 525$ K (15)) and d is the linear temperature coefficient of resistivity at high temperature. The coefficient d is determined from data for $T > 315$ K at $P = 0$, and b is determined from data for $T < 25$ K in the paramagnetic phase at high pressure. For the sample presented in Fig. 2 we find $b/d = 1.95 \pm 0.15(10^{-5}$ K$^{-2})$, in reasonable agreement with the theoretical expectation. The T^3 resistivity in this temperature range (vs. a T^5 form) is typical for metallic samples with residual resistivities $\rho_0 \geq 1$ n$\Omega \cdot$cm (14, 16); our single-crystal Cr is 99.996 + % pure and has $\rho_0 \approx 0.1$ $\mu\Omega \cdot$cm (compared to $\rho_0 \approx$ 1.4 $\mu\Omega \cdot$cm in critically doped Cr:V 3.2% (8)). The electron mean-free path in our samples is estimated to be $\lambda > 400$ Å at base-T for all pressures $P < P_c$, where λ is calculated from the

Author contributions: R.J., Y.F., and T.F.R. designed research; R.J., Y.F., and J.W. performed research; R.J. and T.F.R. analyzed data; and R.J., Y.F., J.W., and T.F.R. wrote the paper.

The authors declare no conflict of interest.

This article is a PNAS Direct Submission.

[1]To whom correspondence should be addressed. E-mail: tfr@uchicago.edu.

PHYSICS

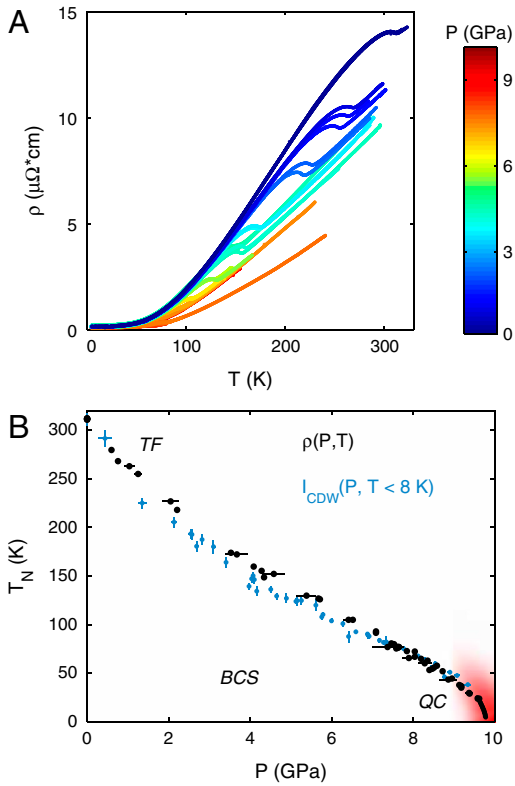

Fig. 1. Data overview and phase diagram for antiferromagnetic Cr under pressure. Data and results shown for all seven samples measured. (*A*) Resistivity $\rho(T)$. (*B*) Antiferromagnetic phase diagram $T_N(P)$. Black = determined directly from $\rho(T)$ curves; Blue = determined indirectly from X-ray measurements of the CDW diffraction intensity I_{CDW} at low temperature (9), from which the phase diagram can be calculated using the harmonic relationship $T_N \propto I_{CDW}{}^{1/4}$. At low pressure the Néel transition is weakly first order, and is anticipated by thermal fluctuations (TF) for $T > T_N$. At low temperature and for pressures $P < 7$ GPa the SDW is well described by the mean-field BCS-like theory and the phase diagram evolves exponentially with P (19, 20). For pressures above 9 GPa this mean-field ground state is continuously suppressed by quantum critical (QC) fluctuations. Red shaded region indicates the quantum critical regime which is the focus of this paper.

measured Hall mobility. We note that the presence of finite quenched disorder in our samples is a necessary precondition for measuring a pressure-dependent residual resistivity. However, the extremely low level of disorder suggests that pure Cr is a benchmark for how closely a QPT in a real solid state system can approach the clean limit.

We plot in Fig. 2*C* the excess resistivity $\Delta\rho/\rho = (\rho - \rho_{PM})/\rho$ calculated from the data in Fig. 2*A* and the ρ_{PM} background (see Fig. 2*B* and *Methods*). As P approaches P_c, it is preferable to analyze data for experimental cuts which are close to perpendicular to the increasingly steep phase diagram $T_N(P)$. We extract such cuts from the data by considering isotherms of $\Delta\rho/\rho$. These isotherms $\Delta\rho/\rho|_T$ are then fit to a power law $\Delta\rho/\rho|_T(P) = a(P_{c,T} - P)^{\beta}$, convolved with a Gaussian that accounts for the finite pressure variation across the sample (see *Methods: Data Analysis in the Critical Regime*). The 5 K isotherm and fit are plotted on the projected $(P, \Delta\rho/\rho)$ plane in Fig. 2*C*, and a scaling plot of the data approaching the low-temperature limit is shown in Fig. 3*A*. The phase diagram is given by the fit parameters $P_{c,T}$, and the exponent β relates to the breakdown of the SDW energy gap and the reemergence of nested Fermi surface area; in the $T \to 0$ limit β directly reflects the critical reconstruction of the Fermi surface.

We present in Fig. 3 the resistivity scaling results for the quantum critical regime. The exponent β converges to 0.24 ± 0.01 for temperatures $T \leq 8$ K (Fig. 3*B*). This exponent speaks to a rapid reconstitution of the Fermi surface that takes place in a narrow quantum critical regime, and stands in contrast to the value $\beta = 2/3$ which is seen at all temperatures in the pressure-driven quantum critical regime in $Cr_{1-x}V_x$, $x = 3.2\%$ (8). β increases with temperature above 8 K, approaching the mean-field value, $\beta = 1/2$, or perhaps even $\beta = 2/3$, as the quantum critical point recedes from sight. However, due to limited data density and the difficulty of modeling ρ_{PM} at higher temperatures, we are not able to follow β to the point at which it settles at a high temperature limit. The crossover in temperature demonstrated in Fig. 3*B* is strongly reminiscent of the crossover from quantum to classical critical scaling that is expected at finite temperatures in a system of itinerant fermions (6), although the applicability of the usual Landau-Ginzburg-Wilson (LGW) critical analysis to the case of nested Fermi surfaces remains in question (7). The critical phase diagram $T_N(P) \propto (P_C - P)^{\gamma}$ is shown in Fig. 3*C*. The exponent γ determined from the two samples is 0.55 ± 0.03 and 0.48 ± 0.05, respectively, giving a best estimate $\gamma = 0.53 \pm 0.03$, consistent with the mean-field expectation, $\gamma = 1/2$, also observed for $Cr_{1-x}V_x$, $x = 3.2\%$.

The critical reconstruction of the nested Fermi surface is further demonstrated by the Hall coefficient, $R_H(P)$. The Hall effect is acutely sensitive to the quantum critical point, changing

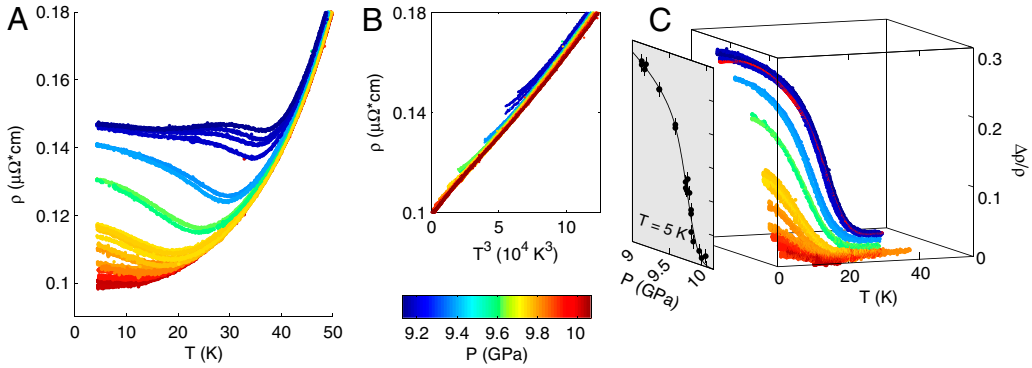

Fig. 2. Data for $9 < P < 10$ GPa for one of the two samples which were measured in detail in the quantum critical regime. The scaling results are the same for both samples, but the different pressure conditions and residual resistivities make it difficult to clearly present raw data for both samples on the same plot. The pressure colorbar applies to *A*–*C*. (*A*) Resistivity $\rho(T)$. (*B*) $\rho(T)$ plotted against T^3 for $T < 50$ K, with each curve truncated just above T_N. Over this temperature range the paramagnetic background $\rho_{PM}(T)$ is dominated by the shown T^3 dependence. (*C*) The magnetic resistivity $\Delta\rho/\rho = (\rho - \rho_{PM})/\rho$, calculated from $\rho(T)$ and the modeled $\rho_{PM}(T)$. Also shown (*dashed red line*) is the McWhan-Rice fit to the lowest pressure curve at 9.13 GPa, for which $T_N = 37.9 \pm 0.03$ K and $g_0/k_B T_N = 1.36 \pm 0.01$ (error bars represent 1-σ variations from the nonlinear fit routine). (*C*, offset) Data and power law fit to the $\Delta\rho/\rho$ isotherm at 5 K. The exponent $\beta = 0.23 \pm 0.03$ and the Gaussian pressure inhomogeneity is 0.24 GPa (FWHM).

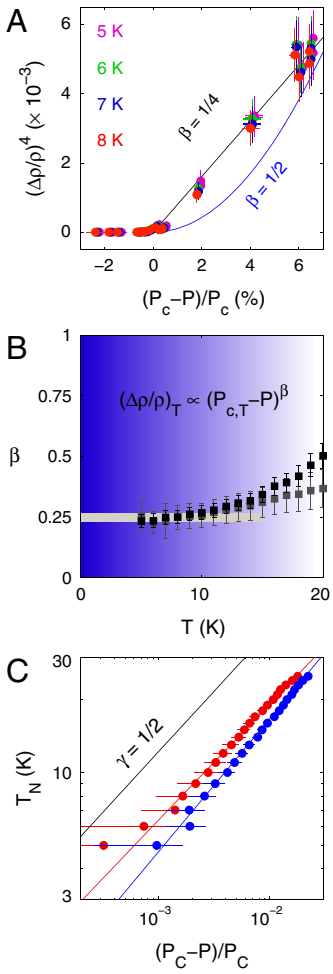

Fig. 3. Quantum critical scaling of the magnetic resistivity $\Delta\rho/\rho$ and the phase boundary T_N. (*A*) Scaling plot of $\Delta\rho/\rho$ shows that the low-temperature isotherms are well described by $\beta = 1/4$ and can be differentiated clearly from the mean-field result, $\beta = 1/2$. (*B*) The $\Delta\rho/\rho$ scaling exponent β converges to 0.24 ± 0.01 for $T \leq 8$ K. Results are shown for both samples (*black* and *gray*, respectively) measured in detail in the critical regime. There is a crossover at higher T to a larger exponent, verging towards approaching either mean-field behavior or the $\beta = 2/3$ found for Cr:V. (*C*) The critical scaling of T_N, which is consistent with the mean-field exponent $\gamma = 1/2$ for both samples (*blue* and *red*, respectively). A nearly constant offset of 0.12 GPa was found between the phase diagrams measured for the two samples. This offset characterizes the systematic uncertainty in our experiment, and although it does not affect error bars in the relative quantity (P-P_c), it does limit the accuracy to which we can determine P_c itself, which we report as 9.71 ± 0.08 GPa.

by 300% across the narrow critical regime at low temperature (Fig. 4). For $P < P_c$, the data can be described by the scaling form $R_H^{-1} \propto (1 - \Delta\rho/\rho)^2$, as predicted for a flat Fermi surface supporting a SDW (17). According to mean-field theory (17, 18), small deviations from ideal nesting will cause both R_H and $\Delta\rho/\rho$ to scale linearly with the SDW energy gap g_0 in the $T \to 0$ limit. Under the conservative assumption that $g_0 \propto T_N$ the data indicate that the gap scales with the mean-field exponent of 1/2, while the Hall coefficient and the excess resistivity behave differently. The non-mean-field scaling which we observe for both R_H and $\Delta\rho/\rho$ implies that the observed critical behavior is driven not by the SDW energy gap, but by fluctuations that restore flat sections of Fermi surface. Moreover, the lengthening of the SDW ordering wavevector Q through the critical regime, in contrast to the monotonically decreasing dependence of Q on P for $P < 7$ GPa, also has been interpreted as evidence for quantum critical fluctuations (9).

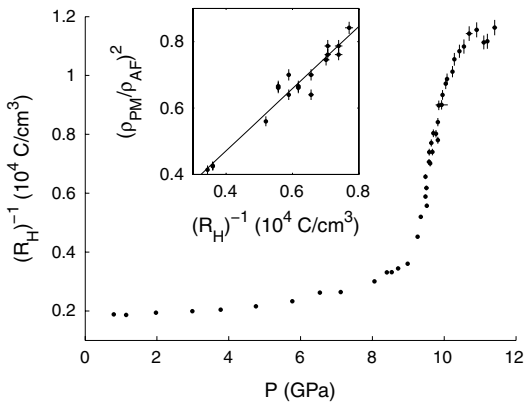

Fig. 4. Overview and critical scaling of the inverse Hall coefficient $R_H^{-1}(P)$ measured at $T = 4.9 \pm 0.4$ K. Inset shows $R_H^{-1} \propto (\rho_{PM}/\rho_{AF})^2$ scaling which is predicted for a flat Fermi surface supporting a SDW; solid line is a linear fit to the data. Resistivity $\rho_{PM}/\rho_{AF} = 1 - \Delta\rho/\rho$ (see *Results*) was recorded at 5.0 ± 0.1 K, and the plotted range is limited to $P < P_c$. The scaling relationship is consistent with $\alpha = \beta \approx 1/4$, where the exponent α describes the $T \to 0$ quantum critical scaling of the Hall coefficient.

Discussion

The complete magnetic phase diagram of Cr can be considered in three parts (illustrated in Fig. 1*B*). At low pressures the Néel transition is weakly discontinuous, and the temperature regime $T > T_N$ is marked by incipient antiferromagnetic fluctuations that go beyond the mean-field theory of the SDW (19). As a function of pressure, however, this BCS-like theory accurately describes the observed exponential dependence of both the phase boundary $T_N(P)$ and the saturated order parameter at low temperature (19, 20). The exponential evolution results from a competition between exchange energy and bandwidth that is tuned by applied pressure while preserving the Fermi surface nesting condition (21). Above 7 GPa the exponential ground state breaks down and the phase diagram approaches the QPT. Finally, at higher pressure the coherent SDW breaks down, quantum critical fluctuations dominate, and the nested Fermi surface reappears at a continuous QPT.

We have shown that the critical scaling of this breakdown is different in pure Cr than in $Cr_{1-x}V_x$, $x = 3.2\%$, which establishes that substitutional disorder is a relevant variable at the pressure-driven QPT. Although the number and identity of relevant variables are well known across the many categories of classical phase transitions, the same is not true for their quantum counterparts. In both the clean and disordered limits we find that the exponent β is distinct from the exponent $\gamma = 1/2$ that describes the scaling of the phase boundary, thus suggesting that the QPTs in both pure and V-doped Cr are driven by fluctuations that couple to the resistivity (18). However the value of β differs between the two cases, as does the scaling $R_H(P) \propto (P_c - P)^\alpha$, which is mean-field in Cr:V and distinctly non-mean-field with an exponent α close to 1/4 in pure Cr. V-doping is more efficient at driving the QPT, in that the phase diagram departs from the exponential curve at a larger T_N (or, equivalently, at a larger SDW coupling constant) for $Cr_{1-x}V_x$ than for pure Cr under pressure (9). Furthermore, with V-doping the body centered cubic lattice expands and the SDW wavevector decreases monotonically, in contrast to the behavior under pressure. This decrease in Q with V-doping results from the fact that the band filling varies with electron-poor doping. However, barring the unrealistic scenario in which pure Cr remains *perfectly* nested at all pressures, this change in band filling is not expected to alter the critical scaling at the QPT. Our scaling results therefore demonstrate that the distinct microscopic effects of chemical doping (or "chemical pressure") and hydrostatic pressure lead to distinct phase transitions, and

indicate that substitutional disorder must be considered a relevant variable for antiferromagnetic QPTs.

For superconducting copper oxides, the relevance of substitutional disorder at the postulated QPT remains an outstanding question. Recent transport measurements on $La_{2-x}Sr_xCuO_4$ at high magnetic fields showed no clear signature of quantum criticality near optimal hole doping, raising the prospect that the tuning parameter of the postulated QPT is substitutional disorder (4). This situation bears similarities to the subject at hand: the scaling of $\Delta\rho/\rho$ with pressure in disordered $Cr_{1-x}V_x$ is broad and extends throughout the entire pressure-temperature plane, while pure Cr has a narrowly defined quantum critical regime. The role of substitutional disorder is somewhat better understood in heavy fermion systems, and well characterized quantum critical points have been found in a number of stoichiometric materials (7, 22). However, the critical spin density wave model, which undoubtedly applies to Cr, does not capture the physics of heavy fermion quantum criticality. Crucially, the lack of local magnetic moments and the absence of effective mass divergences throughout the Brillouin zone separate the QPT in Cr from the heavy fermion examples (23).

Our results also stand in interesting contrast to a body of work on weak itinerant ferromagnets. For these systems, a line of continuous thermal phase transitions terminates at a first-order QPT. The quantum critical regime is inaccessible, but both the magnetic and nonmagnetic ground states are often characterized by strong quantum fluctuations that destabilize the Fermi liquid (3, 5, 24). By contrast, the magnetic ground state of Cr is well described by mean-field theory, with signatures of quantum fluctuations only developing within the narrow quantum critical regime. The outstanding feature common to both Cr and itinerant ferromagnets appears to be a tricritical point in the pressure-temperature plane, where the quartic stiffness of the order parameter passes through zero.

The nature of the quantum fluctuations at the QPT remains an open question. Assuming the applicability of the traditional LGW formalism to nested fermions in three-dimensions, dimensional arguments allow effects beyond mean-field in the quantum regime. The relation $\gamma = z/(d+z-2)$ implies a dynamical exponent $z = 1$ and a scaling dimension $d + z = 4$, which is not over the upper critical dimension (6, 22). Furthermore, the quasi-one-dimensional dispersion relation at the nested Fermi surface (which is the origin of the $R_H^{-1} \propto (1-\Delta\rho/\rho)^2$ scaling (17)) may result in a reduced effective dimension for the critical fluctuations, as has been observed for quantum critical heavy fermion systems (25). The critical reconstruction of the nested Fermi surface in Cr is accompanied by the reemergence of nested fermions with greatly enhanced exchange interactions and as the quantum critical point is uncovered, it drives a weak coupling BCS-like state towards strong-coupling physics (19, 26). The persistence of strongly interacting fermions above P_c also opens the possibility for the ground state that replaces the SDW to be characterized by short-coherence length pairing, akin to the BCS-BEC (Bose Einstein condensate) crossover observed in ultracold gasses, or to a pseudogap-like state of dynamical pair fluctuations.

Methods

Magnetotransport in a Diamond Anvil Cell at Cryogenic Temperatures. All measurements were performed in a low-temperature diamond anvil cell equipped with a He gas membrane for fine pressure control. The pressure medium was a methanol:ethanol 4:1 mixture. Pressure was measured in situ using the ruby fluorescence method. The pressure P is calculated from the wavelength λ of the ruby R_1 fluorescence by $P = A \cdot \ln(\lambda/\lambda_0)$, where λ_0 is the (temperature-dependent) R_1 wavelength at ambient pressure. A has been calibrated directly (12) at 5 K ($A_{5\,K} = 1{,}762 \pm 13$ GPa) and room-T ($A_{295\,K} = 1{,}868$ GPa). To interpolate between these two temperatures we assume that A is constant up to 100 K, above which it varies linearly with temperature, in qualitative accordance with the temperature dependence of the bulk modulus of Al_2O_3. Resistivity ρ and Hall coefficient R_H were measured in the four probe van der Pauw geometry on single-crystal Cr plates using an ac resistance bridge. R_H was derived from data taken in the range $-3{,}500 < H < 3{,}500$ Oe, which is in the low-field limit for all pressures. The microscopic samples, size $(200 \times 200 \times 40)\ \mu m^3$ with (111)-oriented faces, were derived from large Cr single-crystal discs (Alfa Aesar, 99.996 + %) by a procedure described elsewhere (27). The gold leads were spot-welded to the sample and insulated from the metallic gasket using a mixture of alumina powder and epoxy.

McWhan-Rice Model. For pressures up to ~0.3 GPa below P_c the phase diagram was determined by fitting $\Delta\rho/\rho$ to the McWhan-Rice model (13). This model has three free parameters: the Néel temperature T_N, the $T \to 0$ energy gap g_0, and the magnetic Fermi surface fraction q (note the typo in Eq. 6 of ref. 13, where $E^{3/2}$ is written instead of E^3; for the correct expression see Eq. 6.16 of ref. 28). We implemented this model with an additional free parameter dT_N which describes the width of a Gaussian distribution in T_N. This convolution allows for pressure inhomogeneity and is valid as long as the variation in T_N with pressure is approximately linear over the range dT_N. The convolution was implemented numerically, holding q constant and scaling g_0 linearly with T_N. Modeling $\rho_{PM}(T)$ is easy at low temperatures (approximately $T_N < 50$ K or $P > 8.8$ GPa), where it obeys the expected form $\rho_{PM}(T) = \rho_0 + bT^3 + cT^5$ and the T^3 dependence dominates (14, 16). In this regime the McWhan-Rice fit parameters are robust. At higher T modeling $\rho_{PM}(T)$ is difficult, and the McWhan-Rice fit results for g_0 and q are strongly correlated with the form assumed for $\rho_{PM}(T)$. The result for T_N, however, remains robust. As a check we also estimated T_N from $\rho(T)$ by simply finding the temperature at which $\rho(T)$ has the most negative slope. This point is assumed to correspond to that temperature at which the energy gap $g(T)$ grows the fastest, which is identified with T_N. For all $P < 9$ GPa the discrepancy between these results and the McWhan-Rice approach is less than the size of the data points in Fig. 1*B*; for $P > 9$ GPa this simpler technique fails due to the increasing influence of the pressure inhomogeneity as the phase diagram steepens near P_c.

Data Analysis in the Critical Regime. For pressures within ~0.3 GPa of P_C the McWhan-Rice fits fail for two reasons. First, our lowest measurement temperature of 4.5 K is too high for the $\Delta\rho/\rho$ form to fully develop (Fig. 2*C*), and as a result the fit parameters are poorly determined. Second, the finite pressure inhomogeneity produces a smearing of T_N that diverges at P_c. It is preferable to consider the isotherms $\Delta\rho/\rho|_T$, which are fit to a power law $\Delta\rho/\rho|_T(P) = a(P_{c,T} - P)^\beta$ convolved with a Gaussian pressure distribution. The 5 K isotherm and best-fit curve are shown in Fig. 2*C*, and a scaling plot of the data approaching the low-temperature limit is shown in Fig. 3*A*. The critical exponents $\beta(T)$ are plotted in Fig. 3*B*, and the fit parameters $P_{c,T}$ define the phase diagram which is plotted in Fig. 3*C*.

For the two samples studied in fine detail in the critical regime, the best-fit FWHM of the Gaussian pressure distribution was 0.24 and 0.33 GPa, respectively, for the $T = 5$ K data. For a given sample this fit parameter is then held constant for fits to all $T > 5$ K isotherms to reduce systematic correlations between fit parameters. The Gaussian pressure distributions correspond to a 2-σ width of 0.43 and 0.58 GPa, respectively, somewhat smaller than the 0.72 GPa base width that was found for the pressure inhomogeneity over a $(200 \times 200)\ \mu m^2$ area in a recent study of the pressure conditions in the same methanol:ethanol medium at 10 GPa and 5 K (12). The pressure condition is characteristic of a given cell assembly and depends mainly on choice of pressure medium and the sample-to-chamber volume ratio. A nearly constant offset of 0.12 GPa of the critical phase boundaries measured for two different samples could result from several systematic issues, most notably the position of the ruby chips (the ruby is positioned to the side of the sample, close to the gasket wall where the pressure gradients are highest).

ACKNOWLEDGMENTS. We acknowledge Arnab Banerjee and Peter Littlewood for enlightening discussions. The work at the University of Chicago was supported by National Science Foundation (NSF) Grant DMR-0907025.

1. Sachdev S (2000) Quantum criticality: competing ground states in low dimensions. *Science* 288:475–480.
2. Dai J, Si Q, Zhu J-X, Abrahams E (2009) Iron pnictides as a new setting for quantum criticality. *Proc Nat'l Acad Sci USA* 106:4118–4121.
3. Pfleiderer C, et al. (2007) Non-Fermi liquid metal without quantum criticality. *Science* 316:1871–1874.
4. Cooper RA, et al. (2009) Anomalous criticality in the electrical resistivity of $La_{2-x}Sr_xCuO_4$. *Science* 323:603–607.

5. Smith RP, et al. (2008) Marginal breakdown of the Fermi-liquid state on the border of metallic ferromagnetism. *Nature* 455:1220–1223.
6. Millis AJ (1993) Effect of a nonzero temperature on quantum critical points in itinerant fermion systems. *Phys Rev B* 48:7183–7196.
7. Löhneysen HV, Rosch A, Vojta M, Wölfle P (2007) Fermi-liquid instabilities at magnetic quantum phase transitions. *Rev Mod Phys* 79:1015–1075.
8. Lee M, Husmann A, Rosenbaum TF, Aeppli G (2004) High resolution study of magnetic ordering at absolute zero. *Phys Rev Lett* 92:187201.
9. Jaramillo R, et al. (2009) Breakdown of the Bardeen-Cooper-Schrieffer ground state at a quantum phase transition. *Nature* 459:405–409.
10. Yeh A, et al. (2002) Quantum phase transition in a common metal. *Nature* 419:459–462.
11. Overhauser AW (1962) Spin density waves in an electron gas. *Phys Rev* 128:1437–1452.
12. Feng Y, Jaramillo R, Wang J, Ren Y, Rosenbaum TF (2010) High pressure techniques for condensed matter physics at low temperature. *Rev Sci Instrum* 81:041301.
13. McWhan DB, Rice TM (1967) Pressure dependence of itinerant antiferromagnetism in chromium. *Phys Rev Lett* 19:846–849.
14. Campbell IA, Caplin AD, Rizzuto C (1971) Momentum nonconservation and the low-temperature resistivity of alloys. *Phys Rev Lett* 26:239–242.
15. Diana M, Mazzone G (1972) Absolute X-ray measurement of the atomic scattering factor of chromium. *Phys Rev B* 5:3832–3836.
16. Caplin AD, Rizzuto C (1970) Breakdown of Matthiessen's rule in aluminum alloys. *Journal of Physics C: Solid State Physics* 3:L117–L120.
17. Norman MR, Qimiao S, Bazaliy YB, Ramazashvili R (2003) Hall effect in nested antiferromagnets near the quantum critical point. *Phys Rev Lett* 90:116601.
18. Bazaliy YB, Ramazashvili R, Si Q, Norman MR (2004) Magnetotransport near a quantum critical point in a simple metal. *Phys Rev B* 69:144423.
19. Jaramillo R, et al. (2008) Chromium at high pressures: weak coupling and strong fluctuations in an itinerant antiferromagnet. *Phys Rev B* 77:184418.
20. Feng Y, et al. (2007) Pressure-tuned spin and charge ordering in an itinerant antiferromagnet. *Phys Rev Lett* 99:137201.
21. Jaramillo R, Feng Y, Rosenbaum TF (2010) Diffraction line-shapes, Fermi surface nesting, and quantum criticality in antiferromagnetic chromium at high pressure. *J App Phys* 107:09E116.
22. Varma CM, Nuzzinov Z, Saarloos WV (2002) Singular or non-Fermi liquids. *Phys Rep* 361:267–417.
23. Hayden SM, Doubble R, Aeppli G, Perring TG, Fawcett E (2000) Strongly enhanced magnetic excitations near the quantum critical point of $Cr_{1-x}V_x$ and why strong exchange enhancement need not imply heavy fermion behavior. *Phys Rev Lett* 84:999–1002.
24. Pfleiderer C (2007) On the identification of Fermi-liquid behavior in simple transition metal compounds. *J Low Temp Phys* 147:231–247.
25. Schroder A, Aeppli G, Bucher E, Ramazashvili R, Coleman P (1998) Scaling of magnetic fluctuations near a quantum phase transition. *Phys Rev Lett* 80:5623–5626.
26. Aynajian P, et al. (2008) Energy gaps and Kohn anomalies in elemental superconductors. *Science* 319:1509–1512.
27. Feng Y, et al. (2005) Energy dispersive X-ray diffraction of charge density waves via a chemical filtering. *Rev Sci Instrum* 76:063913.
28. Jérome D, Rice TM, Kohn W (1967) Excitonic insulator. *Phys Rev* 158:462–475.